ACS Sustainable Chemistry & Engineering

pubs.acs.org/journal/ascecg

Research Article

Ultrafine Antimony Nanocrystals/Phosphorus Pitaya-Like Nanocomposites as Anodes for High-Performance Sodium-Ion Batteries

Xiang-Ting Zheng,[†] Kuan-Ting Chen,[†] Yi-Yen Hsieh, and Hsing-Yu Tuan*

Cite This: *ACS Sustainable Chem. Eng.* 2020, 8, 18535−18544

Read Online

ACCESS | Metrics & More | Article Recommendations | Supporting Information

ABSTRACT: Ultrafine (3−5 nm in diameters) antimony (Sb) nanocrystals embedded in phosphorus (P) pitaya-like nanocomposites (Sb/P composites) were fabricated via a facile chemical precipitation synthesis. In this pitaya-like structure, P as a buffer matrix could effectively mitigate volume expansion/contraction of Sb and enhance the structural integrity during the Na^+-insertion/extraction process. Moreover, P acted as an active material to contribute capacity for the overall active material, resulting in Na-ion storage capacity higher than that of mono-Sb. When regarded as anode materials, Sb/P nanocomposites delivered a capacity of 795.9 mA h g^{-1} and maintained great cyclability (478.1 mA h g^{-1} at 800 mA g^{-1} over 500 cycles). Furthermore, the rate capability (341.5 mA h g^{-1} at 32 A g^{-1}) was better than the reported literature under higher current density. Most importantly, operando X-ray diffraction and ex situ transmission electron microscopy results were carried out to investigate the structural evolutions of Sb/P, indicating the electrochemical mechanism of the Na_3Sb and Na_3P alloys during the cycling process, which imply that both Sb and P in the nanocomposite could react with Na ions completely. This work possesses an innovative material morphology and replaces the general carbon-based buffer matrix with phosphorus so that the pitaya-like Sb/P composites may become a good alternative in a Na-ion system.

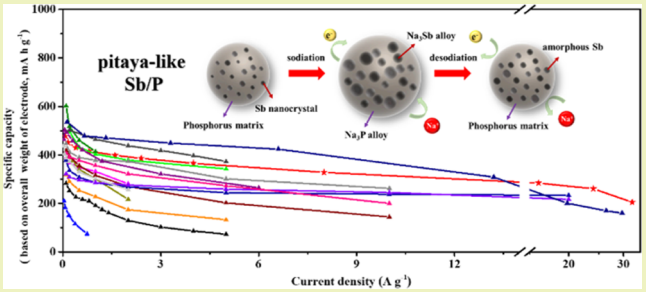

KEYWORDS: *sodium-ion battery, antimony, phosphorus, anode, energy storage, nanocomposites*

INTRODUCTION

Rechargeable energy storages have taken advantage of electric devices and vehicles by virtue of their sufficient energy density and excellent cycle stability.[1−3] Nevertheless, due to the limited Li-metal resource in the earth's crust and high prices of lithium salts, lithium-ion batteries (LIBs) cannot meet the increasing demands for grid-scale energy storages.[4,5] In the new-type secondary batteries, sodium-ion storage has been noticeable as an alternative to LIBs because of its natural abundance, low cost, relatively low redox potential, and feasibility. However, the radius of a Na ion (1.02 Å) larger than that of a Li ion (0.76 Å) leads to a sluggish diffusion kinetic of Na ions and a large volumetric change[6,7] because Na^+ is difficult to insert into appropriate materials (e.g., graphite) and the studies of SIBs focus on designing suitable materials to accommodate Na ions. Therefore, it is necessary to design a unique host for Na^+ applied in a sodium-ion system. To date, alloy-type anode materials have been utilized owing to higher theoretical capacities and suitable sodiation/desodiation potentials (less than 1.0 V) for practical applications of sodium storage (e.g., Ge, Sn, Sb, and P).[8−11] Among them, antimony (Sb) is regarded as a promising material for an SIB system owing to its good electronic conductivity, prospective specific capacity of 660 mA h g^{-1}, and appropriate working voltages between 0.5 and 0.8 V (vs Na/Na^+). However, large volumetric variations (~300% during sodiation) of Sb anodes could cause the pulverization of Sb and the electrolyte consumed by the reforming of the SEI layer, leading to a rapid capacity decrease and a poor cycling performance.

Several effective design concepts have been proposed to enhance electrochemical stability of a series of Sb-based SIB anodes via the nanostructure designs, such as Sb nanocrystals,[12] nanoporous Sb,[13] Sb hollow spheres,[14] Sb nanotubes,[15] few-layer antimony,[16] etc. The nanostructures could minimize the volumetric expansion during cycling and shorten the diffusion distance of Na^+, thereby enhancing the electrochemical stability of Sb electrodes. Moreover, conductive carbon materials imported into Sb nanostructures to form a composite structure (e.g., Sb/carbon fibers composites,[17] yolk-

Received: September 2, 2020
Revised: November 26, 2020
Published: December 9, 2020

Downloaded via NATL TSING HUA UNIV on January 19, 2021 at 04:18:40 (UTC).
See https://pubs.acs.org/sharingguidelines for options on how to legitimately share published articles.

ACS Publications © 2020 American Chemical Society

https://dx.doi.org/10.1021/acssuschemeng.0c06477
ACS Sustainable Chem. Eng. 2020, 8, 18535−18544

shell Sb@C,[18] Sb nanocrystals encapsulated in carbon microspheres,[19] Sb nanorod encapsulated in carbon,[20] Sb/C nanotube composites,[21] and Sb-C nanocomposites[22,23]) can remarkably promote the cycling stability of Sb electrodes. The carbon matrix with strong mechanical strength and high conductivity can alleviate the volumetric change of Sb and provide paths for electron transport. However, the low capacity contribution of the carbon matrix results in a significant reduction of the capacity for the entire electrode material.

To address the above-mentioned issue, we have developed an active material that can contribute to high capacity and serve as a matrix. Phosphorus (P) provides the highest theoretical capacity (2596 mA h g^{-1}) and a suitable operating voltage (<1.0 V) in the overall Na-storage anode materials.[24−26] In this work, we used P as a matrix to confine Sb nanocrystals, which could effectively alleviate the volumetric expansion of Sb and contribute more capacity to the entire anode material. Herein, a chemical precipitation method is developed to synthesize the ultrafine (3−5 nm in diameters) Sb nanocrystals embedded in the P matrix, so-called Sb/P pitaya-like nanocomposites. When evaluated in Na storage, Sb/P electrodes exhibited a capacity of 795.9 mA h g^{-1}, great cycling stability under a current density of 800 mA g^{-1} (over 500 cycles), and an outstanding rate performance (341 mA h g^{-1} at 32 A g^{-1}) better than that of the corresponding studies in a sodium-ion system. Compared with Sb nanocrystals, due to the higher Na^+ diffusivity and the capacitive contribution ratio of the Sb/P active material, it displayed fast dynamic behaviors. In addition, the structural evolution of the Sb/P nanocomposite was examined through *in situ* XRD patterns and *ex situ* TEM images. This result showed the alloying/dealloying processes of Na_3Sb and Na_3P and the structural integrity during the first sodiation/desodiation reactions.

EXPERIMENTAL SECTION

Material Preparation. *Synthesis of Sb Nanocrystals (SbNCs).* SbNCs were synthesized in a three-necked flask under argon gas based on ref 27. First, 0.454 g of $NaBH_4$ (≥98%, Sigma-Aldrich) was dissolved in 25 mL of NMP with constant stirring for 30 min at 60 °C. Meanwhile, 0.684 g of $SbCl_3$ (≥99.95%, Sigma-Aldrich) was dispersed in 5 mL of NMP. Then, the $SbCl_3$ solution was swiftly injected into the reactor, and the solution turned black immediately. After injection, the reactant was instantly cooled down to 25 °C using ice baths. After cooling, the final products were washed with 30 mL of DI water and collected by 8000 rpm centrifugation for 4 min three times.

Synthesis of Sb/P Composites. The synthesis was operated inside an argon-filled glovebox. In this synthesis, 0.065 g of $SbCl_3$ was dissolved in 10 mL of toluene with stirring. Then, 1 mL of $P(SiMe_3)_3$ solution (98%, Strem Chemicals) was added to the reactor. The solution turned dark brown immediately, indicating the formation of the Sb/P composites. After stirring for 30 min, the solution was washed with 30 mL of toluene and 15 mL of ethanol three times with 10 000 rpm for 5 min. The precipitate was heated at 200 °C for 3 h in an argon atmosphere, and finally, pitaya-like Sb/P nanocomposites were obtained.

Characterization. The morphologies of Sb/P nanocomposites were demonstrated using a field-emission scanning electron microscope (HITACHI-SU8010). Furthermore, transmission electron microscopy (TEM, JEOL JEM-ARM200FTH), energy-dispersive X-ray spectroscopy (EDS), high-resolution TEM (HRTEM), selected-area electron diffraction (SAED), and EDS mapping of the Sb/P nanostructures were further used to investigate morphologies. The crystalline structures were recognized by X-ray diffraction (XRD, D8 ADVANCE Eco (Bruker), Cu Kα, λ = 1.54 Å). The chemical constitutions of the Sb/P nanocomposites were carried out by X-ray photoelectron spectroscopy (XPS, PHI Quantera II).

Electrochemical Measurement. The coin-type (CR2032) half cells were assembled in an Ar-filled glovebox. Before electrode preparation, active materials (Sb/P nanocomposites, SbNCs, and commercial Sb) and graphene oxide (GO) were mixed in a ratio of 3:1 (wt %), followed by thermal reduction at 200 °C for 12 h (under argon:hydrogen = 3:1 (vol %)) to form reduced graphene oxide (rGO). The modified Hummers method was used to prepare GO from graphite powder.[28] In a typical electrode preparation, active materials, rGO as a conductive agent and NaCMC binder were prepared in a ratio of 6:2:2 (wt %). The homogeneous slurry was uniformly cast on a Cu foil and dried using a vacuum oven at 100 °C for 2 h. Then, the electrodes were tailored into a diameter of 12 mm with an active mass loading of ∼0.5 mg cm^{-2}. The coin cell was composed of a Sb/P positive electrode, a glass fiber, and a home-made Na-metal foil as a negative electrode. 5 M NaFSI (>98%, TCI America) in dimethoxyethane (DME) was used as an electrolyte. The galvanostatic cycling tests were investigated by Maccor Series 4000 at the voltage range (0.01−2.0 V vs Na/Na^+).

Moreover, in-depth characterizations of the electrodes during an electrochemical process were carried out by cyclic voltammetry (CV), electrochemical impedance spectroscopy (EIS), the galvanostatic intermittent titration technique (GITT), *in situ* XRD, and *ex situ* TEM. CV and EIS measurements were collected by VMP3 (Bio-Logic Science Instruments) at various scan rates and a frequency ranged from 10 kHz to 10 mHz, respectively. The GITT profiles were measured after three activation cycles and a galvanostatic discharge/charge pulse for 10 min, rested by a period of 3 h. An *operando* XRD pattern was operated at a low C rate (current density of 80 mA g^{-1}), with two theta (2θ) ranged from 23 to 50° and a sweep rate of 3° min^{-1}. The structural evolutions at different cutoff states and after 100 cycles were figured out by SEM and *ex situ* TEM.

RESULTS AND DISCUSSION

The schematic diagram of the synthesis is given in Figure 1 for the Sb/P nanocomposites. The pitaya-like Sb/P nanocomposites were developed by a chemical precipitation technique,[29] followed by an annealing treatment. Figure 2a,b presents the morphologies of the nanocomposites identified by FESEM, which were agglomerated at a size of 57.3 ± 20 nm. Figure 2c displays the transmission electron microscopy (TEM) image of Sb/P composites, revealing that the ultrafine nanocrystal Sb is evenly embedded in the P matrix. The nanostructure of Sb/P composites was characterized by high-resolution TEM (HRTEM) with different scales (Figure 2d,e), indicating that the lattice spacing (*d*-spacing) of 0.31 nm was assigned to the (012) plane of Sb. Figure 2f demonstrates the selected-area diffraction (SAED) pattern for a specific region. The diffraction rings were indexed to (012), (104), (110), (202), (024), (116), and (122) planes of Sb. The even distribution of Sb and P elements in Sb/P nanocomposites

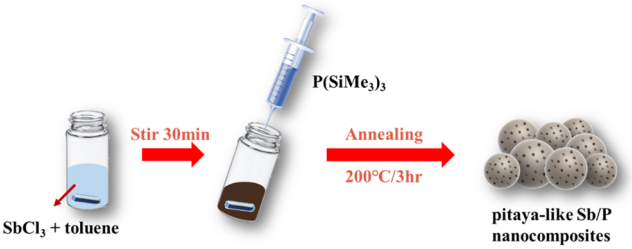

Figure 1. Schematic diagram of the synthesis of pitaya-like Sb/P nanocomposites.

https://dx.doi.org/10.1021/acssuschemeng.0c06477
ACS Sustainable Chem. Eng. 2020, 8, 18535−18544

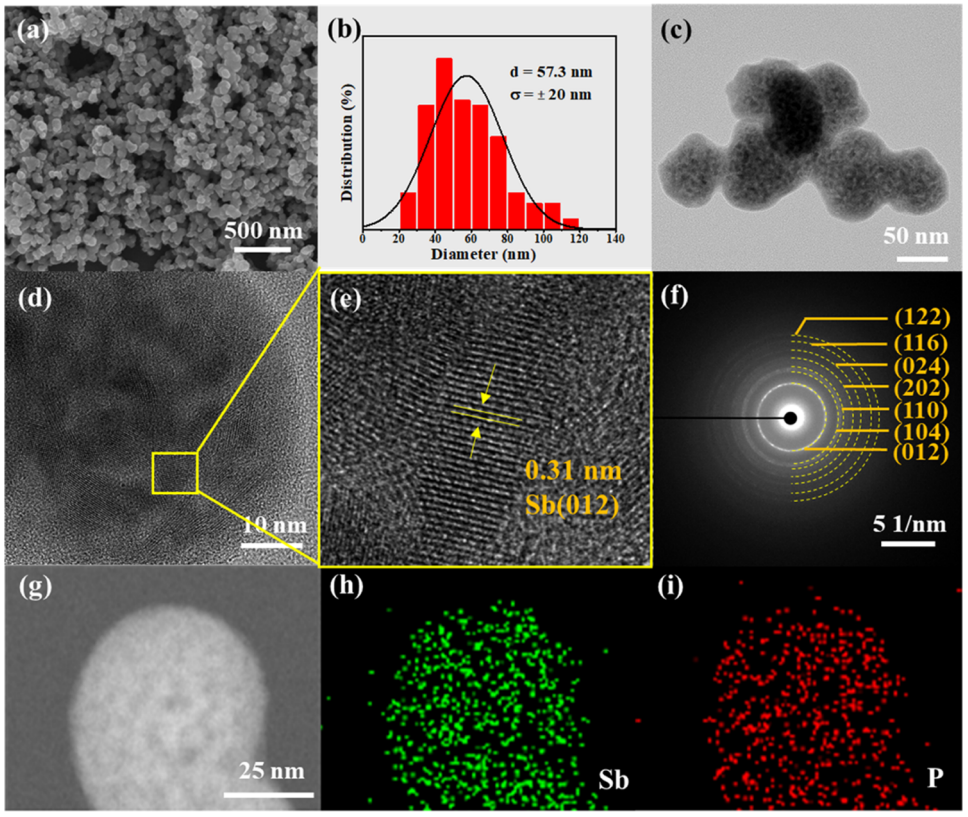

Figure 2. (a) SEM image and (b) size distribution of the Sb/P composites. (c) TEM image (d, e) HRTEM images, (f) SAED pattern, and (g–i) EDS mapping images of the Sb/P composites (green and red represent Sb and P elements, respectively).

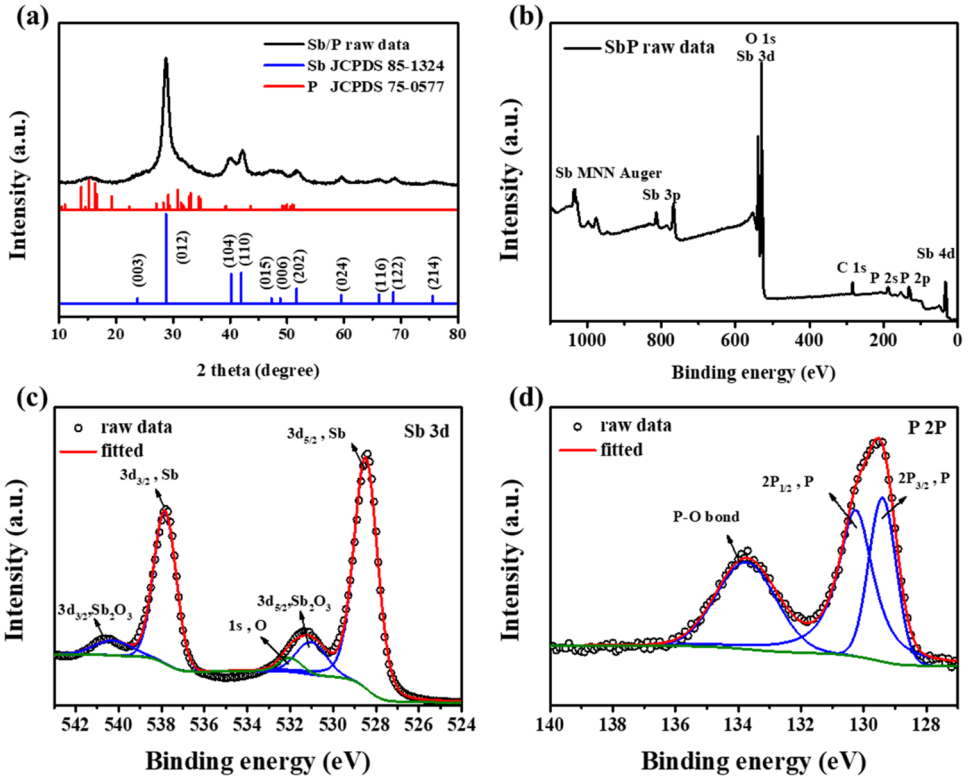

Figure 3. (a) XRD pattern, (b) XPS spectra of the Sb/P composites, and (c) high-resolution spectra of Sb 3d/O 1s and (d) P 2p.

were demonstrated by EDS mapping (Figure 2g–i), consisted of elemental ratios of almost 1:1 (Figure S1).

The crystalline Sb/P powder was further investigated using powder X-ray diffraction (XRD). As shown in Figure 3a, the

https://dx.doi.org/10.1021/acssuschemeng.0c06477
ACS Sustainable Chem. Eng. 2020, 8, 18535–18544

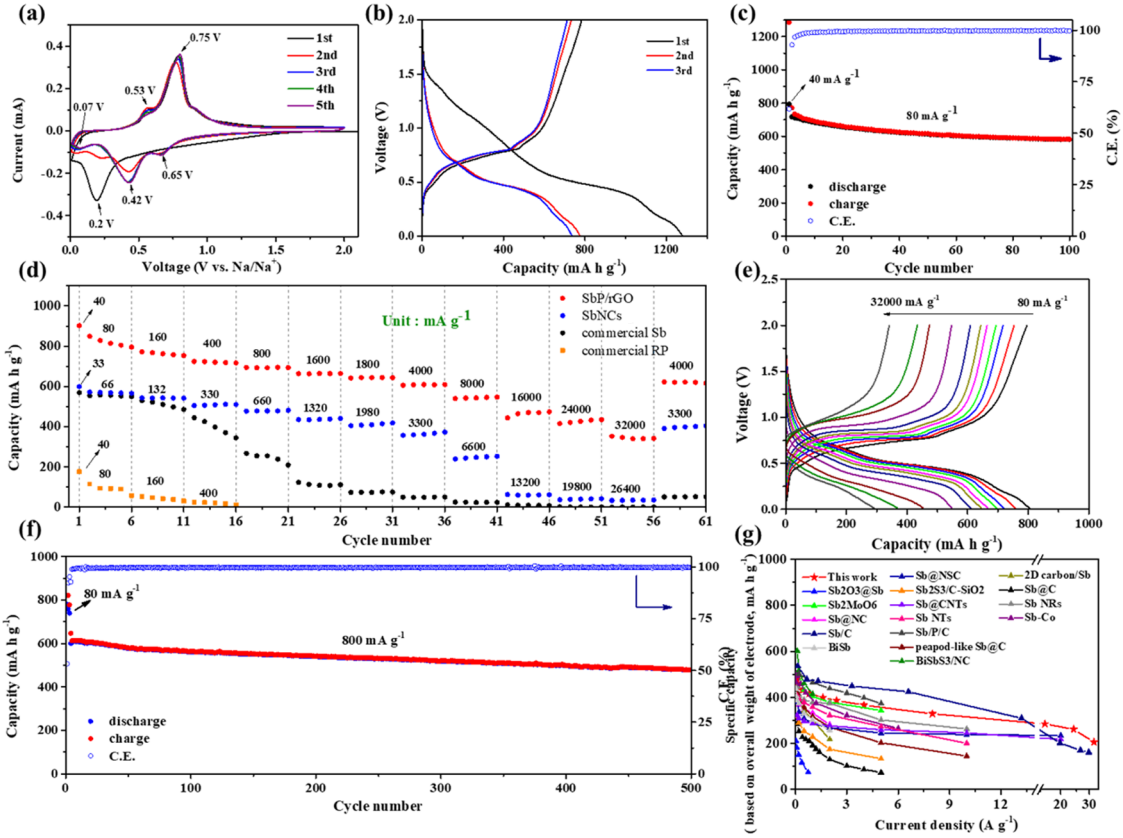

Figure 4. Electrochemical performances of the pitaya-like Sb/P nanocomposites as anodes in SIBs. (a) CV curve at 0.1 mV s^{-1}, (b) galvanostatic discharge/charge curves at 80 mA g^{-1}, (c) cycling performance at 80 mA g^{-1}, (d) rate capabilities of Sb/P, SbNCs, and commercial Sb electrodes at various current densities from 0.1 to 40C, (e) corresponding galvanostatic discharge/charge curves of the Sb/P nanocomposites at different current densities, (f) high-rate cycling performance of the Sb/P nanocomposites at 800 mA g^{-1}, and (g) rate capabilities in this work and the reported literature in Na storages (based on the whole weight of electrodes).

sharp characteristic peaks were probably attributed to the rhombohedral Sb phase (JCPDS 85-1324) and the broad peaks could be assigned to the amorphous phosphorus (JCPDS 75-0577). The diffraction patterns at 23.8, 28.7, 40.2, 42, 47.2, 48.8, 51.7, 59.5, 66.2, 68.7, and 75.5° corresponded to the rhombohedral Sb phases (003), (012), (104), (110), (015), (006), (202), (024), (116), (122), and (214), respectively. Moreover, the impurity peak was not measured in the XRD pattern. The surface chemical state and elemental composition of Sb/P composites were studied by X-ray photoelectron spectroscopy (XPS). Figure 3b displays the XPS survey spectrum of Sb/P composites, which confirmed the existence of Sb and P elements and is consistent with the outcomes of the EDS mapping. Figure 3c exhibits four peaks of Sb $3d_{5/2}$ at ~528.5 eV (Sb^0) and ~531.1 eV (oxidized Sb^{3+}) and Sb $3d_{3/2}$ at ~537.9 eV (Sb^0) and ~540.3 eV (oxidized Sb^{3+}).[30,31] The O 1s peak overlapped with the Sb 3d spectrum and could be distinguished by the Gaussian method at 532 eV. The oxidation signals could be due to the oxidization that occurred on the surface of Sb while being exposed to air. In the P 2p spectrum (Figure 3d), the three deconvoluted peaks situated at 129.4, 130.3, and 133.8 eV were indexed to P $2p_{3/2}$, P $2p_{1/2}$, and the P−O bond, respectively.[32,33] These results suggested that no chemical bonding existed between the elements of Sb and P in the Sb/P nanostructure. For comparison, the unannealed Sb/P composites were also prepared under the same synthesis conditions without an annealing process. The morphologies of the unannealed Sb/P composites were similar to the annealed products (Figure S2). Interestingly, the crystal structure was not observed in HRTEM images, corresponding with the result of the XRD pattern (Figure S3). The three broad diffraction peaks distributed in 13−16, 25−38, and 40−52° corresponded to amorphous phases of Sb and P elements. However, when treated as an anode for Na storage, the unannealed Sb/P composites illustrated a poor cycling performance (Figure S4), which could be affected by the residual byproducts.

Cyclic voltammetry (CV) profiles of pitaya-like Sb/P electrode material were obtained at 0.1 mV s^{-1} (Figure 4a). In the first cathodic scan, a broad peak near 0.2 V could be assigned to the decomposition and growth of an electrolyte and a solid electrolyte interphase (SEI) film, respectively, on the external side of materials. During the following scans, first two cathodic peaks were located at 0.65, and 0.42 V, corresponding to sodiation of Sb and multiple steps of the Na-insertion process from Sb to amorphous/crystalline Na_xSb and hexagonal Na_3Sb. When sweeping to 0.07 V, P was transformed to Na_3P.[34,35] At the anodic scans, two oxidation peaks at 0.53 and 0.75 V corresponded to the dealloying reactions from Na_3P to P and Na_3Sb to Sb, respectively.[36,37] The CV profiles inclined to overlap after the first cycle, indicating that the Sb/P active material possessed high reversibility. Figure 4b displays the galvanostatic charge/discharge measurements of a pitaya-like Sb/P anode at 80 mA g^{-1}. The plateaus at voltage profiles corresponded to the redox reactions of sodium alloying and dealloying processes, which

https://dx.doi.org/10.1021/acssuschemeng.0c06477
ACS Sustainable Chem. Eng. 2020, 8, 18535−18544

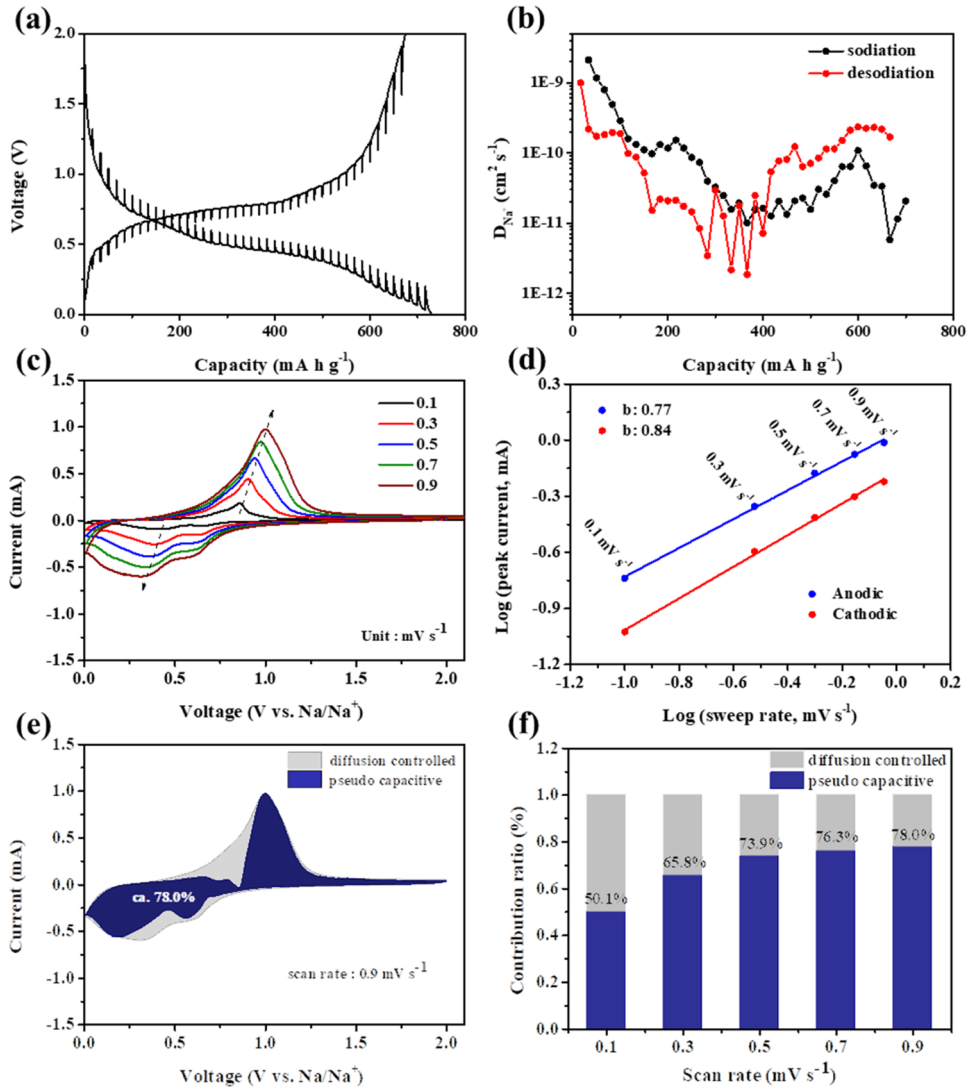

Figure 5. Kinetic behavior analysis toward Na^+ of the Sb/P electrode. (a) GITT curve, the (b) diffusion coefficient of Na^+ ions, (c) CV curves at various scan rates (0.1−0.9 mV s^{-1}), (d) *b* value determination by the corresponding peak current and the sweep rate, (e) distinction between pseudocapacitive and diffusion-controlled contribution at a scan rate of 0.9 mV s^{-1}, and (f) contribution (%) of pseudocapacitive and diffusion-controlled contribution at various scan rates (0.1−0.9 mV s^{-1}).

are in agreement with the above results of CV profiles. The initial discharge and charge specific capacities were 1276.6 and 784.1 mA h g^{-1}, respectively, and the Coulombic efficiency (CE) was 61.4%. The occurrence of capacity loss in the first lap could be affected by the irreversible reactions that formed the SEI film on the external side of active materials and carbon conductive additives.[38,39] The Coulombic efficiency exceeded 99% after several cycles of activation, suggesting a stable SEI film was formed on the Sb/P anode. Figure 4c shows the cycling test of the pitaya-like Sb/P anode at 80 mA g^{-1}. After charging/discharging over 100 cycles, the Sb/P nanocomposites demonstrated a reversible capacity of 580.9 mA h g^{-1}, and the CE of each cycle was higher than 99% after three cycles. When compared with the fifth cycle, the capacity retention reached 83.5%. This result implied that the Sb/P nanostructure had excellent reversibility. Notably, using an optimized electrolyte could make a stable SEI film formed at the first several cycles, thereby improving the cyclability of the electrode and avoiding electrolyte decomposition in the subsequent cycles.[40,41] Besides, the cycling behaviors of the Sb/P electrode were compared with the previous studies of Sb-based composites in SIBs (Table S1). Among them, the Sb/P nanostructure demonstrated great initial capacity because the alloy reaction of P provided more capacity.

To compare the electrochemical performances of the Sb/P nanocomposites, commercial Sb and Sb nanocrystals (SbNCs) were utilized as anode materials in SIBs (Figure S5). Figure 4d shows the rate performances of Sb/P (based on 60 wt % active material, Sb and P), SbNCs, and commercial Sb electrodes at various current densities from 0.1 to 40C. The Sb/P active material (~0.5 mg cm^{-2}) delivered the reversible capacities of 795.9, 753.5, 717, 693.4, 664.3, 643.5, 609.2, 547, 473.8, 434.2, and 341.5 mA h g^{-1} at current densities of 80, 160, 400, 800, 1600, 2400, 4000, 8000, 16 000, 24 000, and 32 000 mA g^{-1}, respectively. Importantly, after returning to 4 A g^{-1}, the Sb/P anode material's capacity could be retrieved to 620 mA h g^{-1}. The corresponding voltage profile (Figure 4e) exhibited the voltage platforms even at 32 A g^{-1} and possessed the least overpotential comparing with other electrodes (Figure S6). The SbNC electrode also demonstrated an excellent rate

https://dx.doi.org/10.1021/acssuschemeng.0c06477
ACS Sustainable Chem. Eng. 2020, 8, 18535−18544

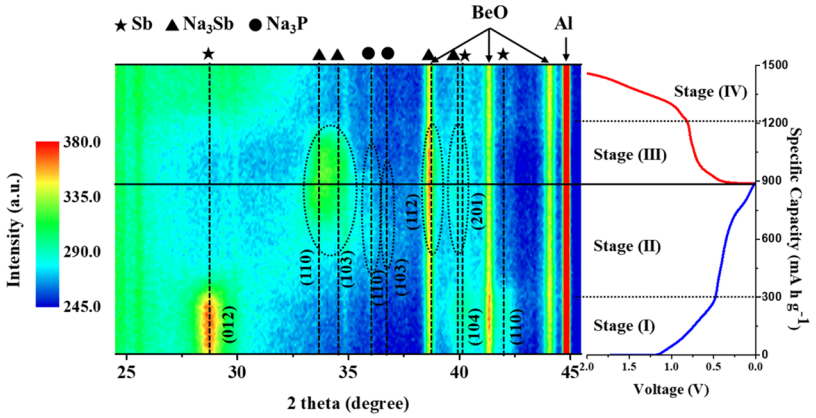

Figure 6. *In situ* XRD pattern of the Sb/P electrode at a C rate of 0.01C (80 mA g^{-1}) during the first cycling process.

capability but could withstand current densities to 6600 mA g^{-1}. Moreover, due to the large volume variations and the Sb pulverizations during charge/discharge cycles, the commercial Sb electrode exhibited a poor rate performance. The superior rate performance of the Sb/P anode corresponded to the ultrafine nanostructure and the high electrical conductivity, which could shorten the Na^+ diffusion length and promote the transmission of electrons. To further clarify the cyclability of Na storage at a higher current region, the cycling performance was obtained at 800 mA g^{-1}. The Sb/P anode presented a specific capacity of 478.1 mA h g^{-1} over 500 cycles, as seen in Figure 4f. Moreover, the good rate capability of the Sb/P anode competed with other materials in Na storage, as seen in Figure 4g and Table S1. Among them, the Sb/P nanocomposites displayed a great rate performance at a high current region (>16 A g^{-1}). Furthermore, the mass loading in this work is smaller than that in many literature, as this result typically leads to better performance; only references with similar loadings were cited for comparing. In addition, the comparison plot of rate performance of each reported literature is based on the overall weight of the electrode involving active materials, conductive agents, and binders.

To explore the in-depth reasons for the outstanding electrochemical performances of Sb/P electrodes, electrochemical impedance spectroscopy (EIS), galvanostatic intermittent titration (GITT), and the CV technique were implemented. The EIS measurements (Figure S7) were used to explore the interfacial electrochemical behaviors of the Sb/P nanocomposites, SbNCs, and commercial Sb. The Nyquist plots consisted of a typical high-frequency semicircle and a low-frequency oblique line. The semicircle represented the charge-transfer resistance (R_{ct}) inside electrode−electrolyte interfaces. The following linear slope means the Warburg impedance, which was associated with the diffusion of Na ions.[42,43] EIS measurements indicated that the Sb/P electrode exhibited the lowest R_{ct} of 380 Ω before cycling with the equivalent circuit, as shown in Figure S7a, suggesting that the unique structure could facilitate the electron transport on the surface. After 50 cycles, the charge-transfer resistances of three electrodes were reduced obviously (Figure S7b). Moreover, the Sb/P electrode demonstrated the lowest R_{ct} of 85 Ω after cycling, which decreased approximately 295 Ω. This result could be attributed to the activation of Sb/P and the formation of a stable SEI film without continual rupturing and reforming.[18,44] Figures 5a and S8a demonstrate the GITT curves of the Sb/P and SbNCs electrodes after three cycle activation, respectively. The GITT measurements were tested under a repetitive control of a current pulse at 100 mA g^{-1} for 10 min, followed by a rest time for 3 h to reach the pseudo-steady state. Based on Fick's second law as follows,[45] the Na^+ diffusion coefficients (D_{Na+}) during the sodiation and desodiation processes were obtained,

$$D_{Na^+} = \frac{4}{\pi\tau}\left(\frac{m_B V_m}{M_B S}\right)^2\left(\frac{\Delta E_S}{\Delta E_\tau}\right)^2 \quad (1)$$

where τ means the time of the pulse current, m_B, M_B, and V_m represent the weight, molecule weight, and molar volume of Sb/P in the electrode, respectively, S is the surface area of the electrode, ΔE_S is the deviation of each equilibrium voltage, and ΔE_τ is the deviation voltage during the current pulse. The calculated D_{Na+} (Figures 5b and S8b) were almost in a range of 10^{-10}−10^{-12} cm^2 s^{-1}, which were similar to Sb-based anode materials.[46,47] Moreover, D_{Na+} of the Sb/P electrode were generally faster than the SbNC electrode at most sodiation and desodiation states, revealing the faster Na-ion kinetic behavior in the Sb/P nanocomposites.

The CV curves at different sweeping rates from 0.1 to 0.9 mV s^{-1} were executed, as shown in Figure 5c. The obvious anodic and cathodic peaks at different scan rates were attributed to Faraday reactions. On the basis of the power law, the relationship between the peak current (i) and the scan rate (v) was presented as below.[48,49]

$$i = av^b \quad (2)$$

b values were calculated by the linear regression of log(i) versus log(v). Typically, the b value adjacent to 0.5 represented an ideal diffusion-controlled model, and the b value near 1 demonstrated a capacitive-controlled behavior. For the Sb/P electrode, b values of cathodic and anodic peaks were given at about 0.84 and 0.77 (Figure 5d), respectively, suggesting that the kinetic behavior tended toward a capacitive contribution process. In addition, the b value of the SbNC electrode was lower than 0.75 (Figure S9a,b), indicating that the reaction kinetics of the SbNC anode was dominated by diffusion-controlled contribution. The Sb/P electrode possessed more capacitive kinetic behavior than the SbNC electrode, which could attain an excellent rate capability. Based on Dunn's method, a quantitative analysis could separate the total storage capacity into capacitive-controlled (k_1v) and diffusion-dominated ($k_2v^{1/2}$) contributions.[50,51]

https://dx.doi.org/10.1021/acssuschemeng.0c06477
ACS Sustainable Chem. Eng. 2020, 8, 18535−18544

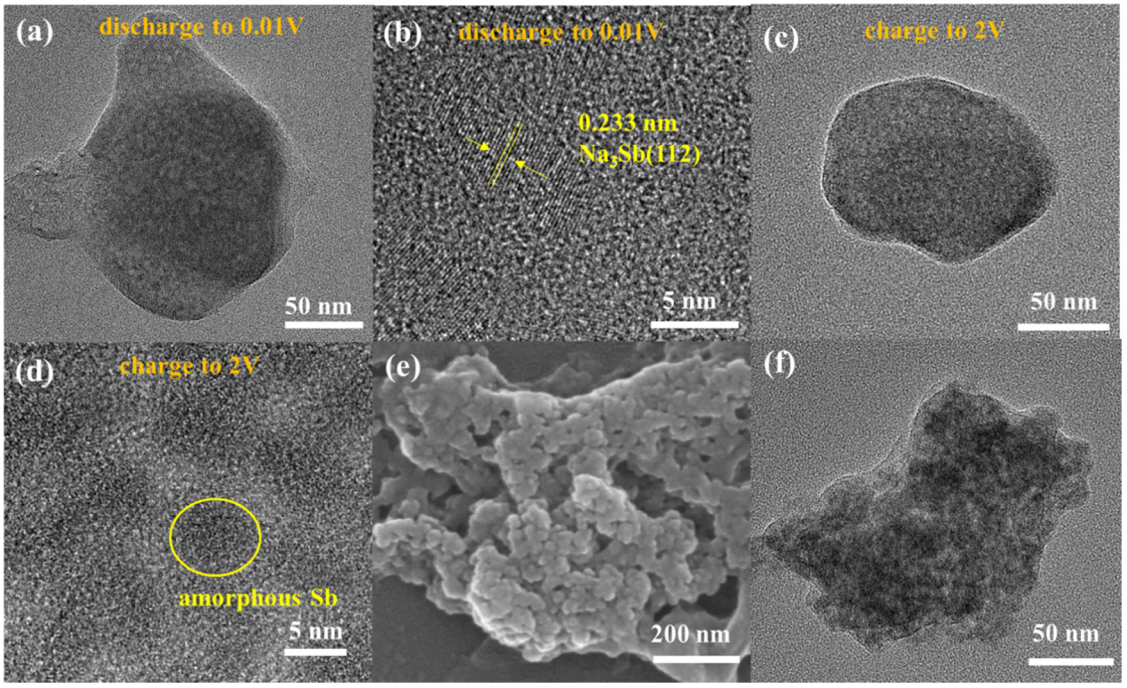

Figure 7. Structural evolutions of the Sb/P nanocomposites at different charge/discharge states. *Ex situ* TEM images (a, b) at the first fully discharged state and (c, d) at the first fully charged state. (e) *Ex situ* SEM image and (f) *ex situ* TEM image after 100 cycles.

$$i(V) = k_1 v + k_2 v^{1/2} \tag{3}$$

Figure 5e shows the proportions between diffusion and surface-capacitive contributions from the CV profiles of the Sb/P anode at 0.9 mV s^{-1}. The capacitive contributions of the Sb/P electrode at various scan rates are shown in Figure 5f. When the scan rate was increased, the capacitive contributions reached a maximum of 78% at 0.9 mV s^{-1}. The high pseudocapacitive contribution ratio occupied most of Na storage, revealing the fast electron and Na-ion transport in the Sb/P electrode materials. Meanwhile, the quantitative capacitive contribution was also calculated for the SbNC electrode, as shown in Figure S9c,d. The result showed diffusion-dominated and less storage from capacitive contribution. Moreover, the overall proportions of capacitive contributions of Sb/P at various sweep rates were much higher than those of SbNCs, which could be attributed to the excellent rate performance.

To further understand the structural evolution[52] and the reaction mechanism of Sb/P composites underwent in sodiation/desodiation, *in situ* XRD was implemented for the initial cycle at 80 mA g^{-1}. Figure 6 demonstrates the *in situ* XRD pattern of the Sb/P anode, and the contour plot was used to clearly distinguish each reaction state by different colors. Red and blue represented the highest and lowest intensity of diffraction peaks, respectively. The strong intensity peaks located at 38.7, 41.4, and 44.1° corresponded to BeO, and the peak at 44.7° was attributed to an Al foil. The XRD result of the fresh electrode was similar to the Sb/P powder with the strong peaks of Sb at 28.7, 40.2, and 42°. In stage I (discharge from OCP to ~0.5 V), the strong XRD peaks disappeared from the (012), (104), and (110) planes, suggesting the alloying reaction and the occurrence of Na_xSb and Na_xP. When the anode was fully discharged to 0.01 V (stage II, from ~0.5 to 0.01 V), the new peaks that appeared at 33.4, 34.3, 38.6, and 40° could be assigned to the alloy of Na_3Sb (JCPDS 74-1162), as well as the peaks at 36 and 37° could be indexed to the formation of Na_3P (JCPDS 74-1164). This phenomenon implied that both Sb and P elements in the nanostructure could react with Na ions, and thus, providing high capacity more than other Sb-based electrodes in the SIBs. During charging back to ~0.8 V (stage III), the peaks of Na_3Sb and Na_3P vanished gradually, implying the dealloying processes of Na_3Sb and Na_3P. When the cell was fully charged (stage IV, from ~0.8 to 2 V), the XRD peaks transferred to the initial positions. No sharp peaks of Sb were observed, suggesting the formation of amorphous Sb after the first sodiation/desodiation process.[20] Therefore, the mechanism for Na-insertion/extraction of the Sb/P could be depicted as follows

The discharge process:

$$\mathrm{Sb} + (3 - x)\mathrm{Na}^+ + (3 - x)\mathrm{e}^- \rightarrow \mathrm{Na}_{3-x}\mathrm{Sb}(x = 1 - 3) \tag{4}$$

$$\mathrm{P} + (3 - x)\mathrm{Na}^+ + (3 - x)\mathrm{e}^- \rightarrow \mathrm{Na}_{3-x}\mathrm{P}(x = 1 - 3) \tag{5}$$

The charge process:

$$\mathrm{Na_3Sb} \rightarrow 3\mathrm{Na}^+ + 3\mathrm{e}^- + \mathrm{Sb} \tag{6}$$

$$\mathrm{Na_3P} \rightarrow 3\mathrm{Na}^+ + 3\mathrm{e}^- + \mathrm{P} \tag{7}$$

Additionally, the *ex situ* TEM images were utilized to support the structural evolution of the Sb/P active material from *in situ* XRD. Figure 7 demonstrates the *ex situ* TEM and HRTEM images at different cutoff states of 0.01 and 2 V. As shown in Figure 7a, P as the matrix could buffer the dramatic expansion of the volume, even if the active material underwent the alloying reactions after fully sodiation. The lattice fringes of the pristine Sb/P powder were not observed and the d-spacing of 0.233 nm was identified by HRTEM (Figure 7b), corresponding to the (112) plane of the Na_3Sb alloy. When the voltage was fully charged to 2 V, the Sb/P electrode

https://dx.doi.org/10.1021/acssuschemeng.0c06477
ACS Sustainable Chem. Eng. 2020, 8, 18535−18544

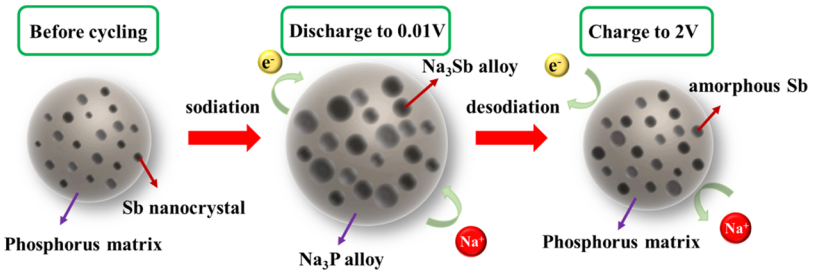

Figure 8. Schematic illustration of the structural evolutions for the pitaya-like Sb/P nanocomposites during the sodiation/desodiation process.

material could return to a structure similar to the initial shape (Figure 7c), revealing that the P matrix could avoid the pulverization of active material after the sodiation/desodiation process. In addition, the HRTEM image exhibited the amorphous structure after the first cycle, as shown in Figure 7d, consistent with the result of *in situ* XRD. Furthermore, the morphological divergences of the Sb/P nanocomposites after 100 cycles were carried out by the *ex situ* SEM and TEM measurements, as shown in Figure 7e,f. Due to different potentials of Sb and P, abrupt simultaneous expansion of contraction of the whole electrode is avoided and causes an improved cyclability.[53] Furthermore, the amorphous matrix (e.g., phosphorus−carbon matrix) could provide sufficient conductivity that promoted great electrical contact and reduced volume expansion in the connections between the phosphorus and the Cu foil (current collector).[54] Meanwhile, the incorporation of P and Na_3P phases, which are repeatedly transferred during cycling could prevent agglomeration and disperse the mechanical stress to suppress phase segregation.[55] The construction of the Sb/P anode material was maintained and no pulverization or deformation was observed after repetitive sodiation/desodiation processes. Therefore, the Sb/P composites with strong mechanical stability could alleviate the volumetric expansion/extraction of electrode material during cycling, and thus, exhibited long cycling stabilities.

In accordance with the above-mentioned analysis, the excellent electrochemical performances of the pitaya-like Sb/P nanocomposites could be attributable to these reasons: first, the nanostructure of the Sb/P anode material could shorten the diffusion length of Na^+. Second, P participated in the electrochemical reactions that formed the Na_3P alloy, thereby increasing the anode capacity to almost 800 mA h g^{-1}. Third, P also acted as a matrix, which could effectively inhibit the volumetric expansion during the Na-insertion/extraction process, as shown in Figure 8. Moreover, the matrix could alleviate the cracking of the Sb/P nanocomposites and maintain structural integrity. Fourth, a stable SEI layer was formed around the external side of Sb/P material, and in each charge/discharge state, the Na^+ diffusion coefficient and capacitive contributions were higher than those of the SbNC anode. Based on these advantages, the transmission speed of Na^+ and electrons could be promoted so that the Sb/P electrode demonstrated extraordinary rate performance. Therefore, the pitaya-like Sb/P nanocomposites with a high specific capacity and a superior rate capability could be used as one of the new anode candidates for the development of sodium storages.

CONCLUSIONS

In summary, the pitaya-like ultrafine Sb nanocrystals/P nanocomposites were introduced via a simple chemical precipitation technique. When regarded as anode materials for a sodium-ion system, Sb/P electrodes could deliver a high specific capacity of 795.9 mA h g^{-1}, capacities of 580.9 mA h g^{-1} under 80 mA g^{-1} at sequential 100 cycles, and 478.1 mA h g^{-1} at 800 mA g^{-1} over 500 cycles. Furthermore, the great rate capability with a reversible capacity of 341.5 mA h g^{-1} was demonstrated even under a tremendously higher current region of 32 A g^{-1}. Sb nanocrystals embedded in P possessed high electrical conductivity so that it could reduce the Na-ion diffusion length and promote the Na-storage performance. The P matrix could effectively alleviate the volumetric expansion/extraction of Sb and maintain structural integrity during the cycling process. Moreover, P also participated in the electrochemical reactions and contributed more capacity to the entire active material, which exhibited a higher specific capacity than Sb-based anodes. The alloy mechanisms of structural evolution during cycling were carefully verified by *in situ* XRD and *ex situ* TEM, revealing the sodiation/desodiation process of the Na_3Sb and Na_3P alloys. The phenomenon directly indicated that both Sb and P in the nanostructure could react with Na ions, providing more capacity than other Sb-based electrodes in the SIBs. Furthermore, the measurements of GITT, CV at different scan rates, and EIS were implemented to investigate the kinetic behaviors of the Sb/P electrode. The Sb/P anode demonstrated a relatively low resistance before and after cycling and displayed a higher proportion of capacitive-controlled contribution, suggesting that a stable SEI film was formed and the transport of electrons and Na ions was promoted. Therefore, the novel Sb/P pitaya-like nanocomposites with an outstanding rate capability surpassed the reported Sb-based electrode materials. We believed that the Sb/P pitaya-like nanocomposites could be recognized as a prospective candidate applied as an anode material in sodium energy storage.

ASSOCIATED CONTENT

Supporting Information

The Supporting Information is available free of charge at https://pubs.acs.org/doi/10.1021/acssuschemeng.0c06477.

Supplementary data to this article can be found on the ACS Publications website at DOI:(PDF)

AUTHOR INFORMATION

Corresponding Author

Hsing-Yu Tuan − *Department of Chemical Engineering, National Tsing Hua University, Hsinchu 30013, Taiwan;*

https://dx.doi.org/10.1021/acssuschemeng.0c06477
ACS Sustainable Chem. Eng. 2020, 8, 18535−18544

orcid.org/0000-0003-2819-2270; Email: hytuan@che.nthu.edu.tw

Authors

Xiang-Ting Zheng − *Department of Chemical Engineering, National Tsing Hua University, Hsinchu 30013, Taiwan*

Kuan-Ting Chen − *Department of Chemical Engineering, National Tsing Hua University, Hsinchu 30013, Taiwan*

Yi-Yen Hsieh − *Department of Chemical Engineering, National Tsing Hua University, Hsinchu 30013, Taiwan*

Complete contact information is available at: https://pubs.acs.org/10.1021/acssuschemeng.0c06477

Author Contributions

†X.-T.Z. and K.-T.C contributed equally to this work and share first authorship.

Author Contributions

This manuscript was written through the contributions of all authors. All authors have given their approval for the final version of the manuscript.

Notes

The authors declare no competing financial interest.

■ ACKNOWLEDGMENTS

The authors acknowledge the financial support by the Ministry of Science and Technology through grants MOST 108-2622-8-007-016 and MOST 109-2636-E-007-011.

■ REFERENCES

(1) Tarascon, J.-M.; Armand, M. Issues and challenges facing rechargeable lithium batteries. *Nature* **2001**, *414*, 359−367.

(2) Armand, M.; Tarascon, J.-M. Building better batteries. *Nature* **2008**, *451*, 652−657.

(3) Whittingham, M. S. History, evolution, and future status of energy storage. *Proc. IEEE* **2012**, *100*, 1518−1534.

(4) Yabuuchi, N.; Kubota, K.; Dahbi, M.; Komaba, S. Research development on sodium-ion batteries. *Chem. Rev.* **2014**, *114*, 11636−11682.

(5) Martin, G.; Rentsch, L.; Höck, M.; Bertau, M. Lithium market research−global supply, future demand and price development. *Energy Storage Mater.* **2017**, *6*, 171−179.

(6) Hwang, J.-Y.; Myung, S.-T.; Sun, Y.-K. Sodium-ion batteries: present and future. *Chem. Soc. Rev.* **2017**, *46*, 3529−3614.

(7) Ellis, B. L.; Nazar, L. F. Sodium and sodium-ion energy storage batteries. *Curr. Opin. Solid State Mater. Sci.* **2012**, *16*, 168−177.

(8) Keum, J. K.; Browning, J. F.; Veith, G. M. Germanium as negative electrode material for sodium-ion batteries. *Electrochem. Commun.* **2013**, *34*, 41−44.

(9) Liu, Y.; Zhang, N.; Jiao, L.; Chen, J. Tin nanodots encapsulated in porous nitrogen-doped carbon nanofibers as a free-standing anode for advanced sodium-ion batteries. *Adv. Mater.* **2015**, *27*, 6702−6707.

(10) Chang, W.-C.; Tseng, K.-W.; Tuan, H.-Y. Solution synthesis of iodine-doped red phosphorus nanoparticles for lithium-ion battery anodes. *Nano Lett.* **2017**, *17*, 1240−1247.

(11) Xie, J.; Xia, J.; Yuan, Y.; Liu, L.; Zhang, Y.; Nie, S.; Wang, X.; et al. Sb2S3 embedded in carbon−silicon oxide nanofibers as high-performance anode materials for lithium-ion and sodium-ion batteries. *J. Power Sources* **2019**, *435*, No. 226762.

(12) He, M.; Kravchyk, K.; Walter, M.; Kovalenko, M. V. Monodisperse antimony nanocrystals for high-rate Li-ion and Na-ion battery anodes: nano versus bulk. *Nano Lett.* **2014**, *14*, 1255−1262.

(13) Liu, S.; Feng, J.; Bian, X.; Liu, J.; Xu, H. The morphology-controlled synthesis of a nanoporous-antimony anode for high-performance sodium-ion batteries. *Energy Environ. Sci.* **2016**, *9*, 1229−1236.

(14) Hou, H.; Jing, M.; Yang, Y.; Zhu, Y.; Fang, L.; Song, W.; Pan, C.; Yang, X.; Ji, X. Sodium/lithium storage behavior of antimony hollow nanospheres for rechargeable batteries. *ACS Appl. Mater. Interfaces* **2014**, *6*, 16189−16196.

(15) Liu, Y.; Zhou, B.; Liu, S.; Ma, Q.; Zhang, W.-H. Galvanic replacement synthesis of highly uniform Sb nanotubes: reaction mechanism and enhanced sodium storage performance. *ACS nano* **2019**, *13*, 5885−5892.

(16) Tian, W.; Zhang, S.; Huo, C.; Zhu, D.; Li, Q.; Wang, L.; Ren, X.; Xie, L.; Guo, S.; Chu, P. K.; et al. Few-layer antimonene: anisotropic expansion and reversible crystalline-phase evolution enable large-capacity and long-life Na-ion batteries. *ACS Nano* **2018**, *12*, 1887−1893.

(17) Wu, L.; Hu, X.; Qian, J.; Pei, F.; Wu, F.; Mao, R.; Ai, X.; Yang, H.; Cao, Y. Sb−C nanofibers with long cycle life as an anode material for high-performance sodium-ion batteries. *Energy Environ. Sci.* **2014**, *7*, 323−328.

(18) Liu, J.; Yu, L.; Wu, C.; Wen, Y.; Yin, K.; Chiang, F.-K.; Hu, R.; Liu, J.; Sun, L.; Gu, L.; et al. New nanoconfined galvanic replacement synthesis of hollow Sb@ C yolk−shell spheres constituting a stable anode for high-rate Li/Na-ion batteries. *Nano Lett.* **2017**, *17*, 2034−2042.

(19) Qiu, S.; Wu, X.; Xiao, L.; Ai, X.; Yang, H.; Cao, Y. Antimony nanocrystals encapsulated in carbon microspheres synthesized by a facile self-catalyzing solvothermal method for high-performance sodium-ion battery anodes. *ACS Appl. Mater. Interfaces* **2016**, *8*, 1337−1343.

(20) Cui, C.; Xu, J.; Zhang, Y.; Wei, Z.; Mao, M.; Lian, X.; Wang, S.; Yang, C.; Fan, X.; Ma, J.; et al. Antimony Nanorod Encapsulated in Cross-Linked Carbon for High-Performance Sodium Ion Battery Anodes. *Nano Lett.* **2018**, *19*, 538−544.

(21) Liu, Z.; Yu, X.-Y.; Lou, X. W. D.; Paik, U. Sb@ C coaxial nanotubes as a superior long-life and high-rate anode for sodium ion batteries. *Energy Environ. Sci.* **2016**, *9*, 2314−2318.

(22) Qian, J.; Chen, Y.; Wu, L.; Cao, Y.; Ai, X.; Yang, H. High capacity Na-storage and superior cyclability of nanocomposite Sb/C anode for Na-ion batteries. *Chem. Commun.* **2012**, *48*, 7070−7072.

(23) Ramireddy, T.; Sharma, N.; Xing, T.; Chen, Y.; Leforestier, J.; Glushenkov, A. M. Size and composition effects in Sb-carbon nanocomposites for sodium-ion batteries. *ACS Appl. Mater. Interfaces* **2016**, *8*, 30152−30164.

(24) Qian, J.; Wu, X.; Cao, Y.; Ai, X.; Yang, H. High capacity and rate capability of amorphous phosphorus for sodium ion batteries. *Angew. Chem.* **2013**, *125*, 4731−4734.

(25) Kim, Y.; Park, Y.; Choi, A.; Choi, N. S.; Kim, J.; Lee, J.; Lee, K. T.; et al. An amorphous red phosphorus/carbon composite as a promising anode material for sodium ion batteries. *Adv. Mater.* **2013**, *25*, 3045−3049.

(26) Ramireddy, T.; Xing, T.; Rahman, M. M.; Chen, Y.; Dutercq, Q.; Gunzelmann, D.; Glushenkov, A. M. Phosphorus−carbon nanocomposite anodes for lithium-ion and sodium-ion batteries. *J. Mater. Chem. A* **2015**, *3*, 5572−5584.

(27) Walter, M.; Erni, R.; Kovalenko, M. V. Inexpensive antimony nanocrystals and their composites with red phosphorus as high-performance anode materials for Na-ion batteries. *Sci. Rep.* **2015**, *5*, No. 8418.

(28) Shahriary, L.; Athawale, A. A. Graphene oxide synthesized by using modified hummers approach. *Int. J. Renew. Energy Environ. Eng.* **2014**, *2*, 58−63.

(29) Allen, G. C.; Carmalt, C. J.; Cowley, A. H.; Hector, A. L.; Kamepalli, S.; Lawson, Y. G.; Norman, N. C.; Parkin, I. P.; Pickard, L. K. Preparation and characterization of a material of composition BiP and other intergroup 15 element phases. *Chem. Mater.* **1997**, *9*, 1385−1392.

(30) Ruiz, O.; Cochrane, M.; Li, M.; Yan, Y.; Ma, K.; Fu, J.; Wang, Z.; Tolbert, S. H.; Shenoy, V. B.; Detsi, E. Enhanced Cycling Stability of Macroporous Bulk Antimony-Based Sodium-Ion Battery Anodes Enabled through Active/Inactive Composites. *Adv. Energy Mater.* **2018**, *8*, No. 1801781.

(31) Ma, W.; Wang, J.; Gao, H.; Niu, J.; Luo, F.; Peng, Z.; Zhang, Z. A mesoporous antimony-based nanocomposite for advanced sodium ion batteries. *Energy Storage Mater.* **2018**, *13*, 247−256.
(32) Zhou, J.; Liu, X.; Cai, W.; Zhu, Y.; Liang, J.; Zhang, K.; Lan, Y.; Jiang, Z.; Wang, G.; Qian, Y. Wet-chemical synthesis of hollow red-phosphorus nanospheres with porous shells as anodes for high-performance lithium-ion and sodium-ion batteries. *Adv. Mater.* **2017**, *29*, No. 1700214.
(33) Hu, Y.; Li, B.; Jiao, X.; Zhang, C.; Dai, X.; Song, J. Stable Cycling of Phosphorus Anode for Sodium-Ion Batteries through Chemical Bonding with Sulfurized Polyacrylonitrile. *Adv. Funct. Mater.* **2018**, *28*, No. 1801010.
(34) Hou, H.; Jing, M.; Yang, Y.; Zhang, Y.; Zhu, Y.; Song, W.; Yang, X.; Ji, X. Sb porous hollow microspheres as advanced anode materials for sodium-ion batteries. *J. Mater. Chem. A* **2015**, *3*, 2971−2977.
(35) Wen, S.; Zhao, J.; Chen, J.; Yang, J.; Xu, J. BiSbS 3@ N-doped carbon core−shell nanorods as efficient anode materials for sodium-ion batteries. *Dalton Trans.* **2019**, *48*, 10448−10454.
(36) Ye, J.; Xia, G.; Zheng, Z.; Hu, C. (2020). Facile controlled synthesis of coral-like nanostructured Sb_2O_3@ Sb anode materials for high performance sodium-ion batteries. *Int. J. Hydrogen Energy* **2020**, *45*, 9969−9978.
(37) Li, W.; Hu, S.; Luo, X.; Li, Z.; Sun, X.; Li, M.; Liu, F.; Yu, Y. Confined amorphous red phosphorus in MOF-derived N-doped microporous carbon as a superior anode for sodium-ion battery. *Adv. Mater.* **2017**, *29*, No. 1605820.
(38) Wang, J.; Luo, C.; Gao, T.; Langrock, A.; Mignerey, A. C.; Wang, C. An Advanced MoS2/Carbon Anode for High-Performance Sodium-Ion Batteries. *Small* **2015**, *11*, 473−481.
(39) Bommier, C.; Ji, X. Electrolytes, SEI Formation, and Binders: A Review of Nonelectrode Factors for Sodium-Ion Battery Anodes. *Small* **2018**, *14*, No. 1703576.
(40) Eshetu, G. G.; Diemant, T.; Hekmatfar, M.; Grugeon, S.; Behm, R. J.; Laruelle, S.; Armand, M.; Passerini, S. Impact of the electrolyte salt anion on the solid electrolyte interphase formation in sodium ion batteries. *Nano Energy* **2019**, *55*, 327−340.
(41) Pan, H.; Lu, X.; Yu, X.; Hu, Y. S.; Li, H.; Yang, X. Q.; Chen, L. Sodium storage and transport properties in layered Na2Ti3O7 for room-temperature sodium-ion batteries. *Adv. Energy Mater.* **2013**, *3*, 1186−1194.
(42) Pan, J.; Chen, S.; Fu, Q.; Sun, Y.; Zhang, Y.; Lin, N.; Gao, P.; Yang, J.; Qian, Y. Layered-structure SbPO4/reduced graphene oxide: an advanced anode material for sodium ion batteries. *ACS nano* **2018**, *12*, 12869−12878.
(43) He, Y.; Wang, L.; Dong, C.; Li, C.; Ding, X.; Qian, Y.; Xu, L. In-situ rooting ZnSe/N-doped hollow carbon architectures as high-rate and long-life anode materials for half/full sodium-ion and potassium-ion batteries. *Energy Storage Mater.* **2019**, *23*, 35−45.
(44) Ren, W.; Zhang, H.; Guan, C.; Cheng, C. Ultrathin MoS2 nanosheets@ metal organic framework-derived N-doped carbon nanowall arrays as sodium ion battery anode with superior cycling life and rate capability. *Adv. Funct. Mater.* **2017**, *27*, No. 1702116.
(45) Xu, Y.; Zhu, Y.; Liu, Y.; Wang, C. Electrochemical performance of porous carbon/tin composite anodes for sodium-ion and lithium-ion batteries. *Adv. Energy Mater.* **2013**, *3*, 128−133.
(46) Liu, F.; Wang, Y.; Zhang, Y.; Lin, J.; Su, Q.; Shi, J.; Xie, X.; Liang, S.; Pan, A. A Facile Carbon Quantum Dot-Modified Reduction Approach Towards Tunable Sb@ CQDs Nanoparticles for High Performance Sodium Storage. *Batteries Supercaps* **2020**, 463.
(47) Fan, X.-Y.; Jiang, Z.; Huang, L.; Wang, X.; Han, J.; Sun, R.; Gou, L.; Li, D.-L.; Ding, Y.-L. 3D Porous Self-Standing Sb Foam Anode with a Conformal Indium Layer for Enhanced Sodium Storage. *ACS Appl. Mater. Interfaces* **2020**, *12*, 20344−20353.
(48) Chao, D.; Liang, P.; Chen, Z.; Bai, L.; Shen, H.; Liu, X.; Xia, X.; Zhao, Y.; Savilov, S. V.; Lin, J.; et al. Pseudocapacitive Na-ion storage boosts high rate and areal capacity of self-branched 2D layered metal chalcogenide nanoarrays. *ACS Nano* **2016**, *10*, 10211−10219.
(49) Muller, G. A.; Cook, J. B.; Kim, H.-S.; Tolbert, S. H.; Dunn, B. High performance pseudocapacitor based on 2D layered metal chalcogenide nanocrystals. *Nano Lett.* **2015**, *15*, 1911−1917.
(50) Chen, C.; Wen, Y.; Hu, X.; Ji, X.; Yan, M.; Mai, L.; Hu, P.; Shan, B.; Huang, Y. Na+ intercalation pseudocapacitance in graphene-coupled titanium oxide enabling ultra-fast sodium storage and long-term cycling. *Nat. Commun.* **2015**, *6*, 1−8.
(51) Augustyn, V.; Come, J.; Lowe, M. A.; Kim, J. W.; Taberna, P.-L.; Tolbert, S. H.; Abruña, H. D.; Simon, P.; Dunn, B. High-rate electrochemical energy storage through Li+ intercalation pseudocapacitance. *Nat. Mater.* **2013**, *12*, 518−522.
(52) Huang, Y.; Zhu, C.; Zhang, S.; Hu, X.; Zhang, K.; Zhou, W.; Zeng, H.; et al. Ultrathin bismuth nanosheets for stable Na-ion batteries: clarification of structure and phase transition by in situ observation. *Nano Lett.* **2019**, *19*, 1118−1123.
(53) Sultana, I.; Rahman, M. M.; Liu, J.; Sharma, N.; Ellis, A. V.; Chen, Y.; Glushenkov, A. M. Antimony-carbon nanocomposites for potassium-ion batteries: Insight into the failure mechanism in electrodes and possible avenues to improve cyclic stability. *J. Power Sources* **2019**, *413*, 476−484.
(54) Zhang, M.; Ouyang, L.; Zhu, M.; Fang, F.; Liu, J.; Liu, Z. A phosphorus and carbon composite containing nanocrystalline Sb as a stable and high-capacity anode for sodium ion batteries. *J. Mater. Chem. A* **2020**, *8*, 443−452.
(55) Liu, C.; Han, X.; Cao, Y.; Zhang, S.; Zhang, Y.; Sun, J. Topological construction of phosphorus and carbon composite and its application in energy storage. *Energy Storage Mater.* **2019**, *20*, 343−372.

https://dx.doi.org/10.1021/acssuschemeng.0c06477
ACS Sustainable Chem. Eng. 2020, 8, 18535−18544